

Article

# Classification of Fracture and Normal Shoulder Bone X-Ray Images Using Ensemble and Transfer Learning With Deep Learning Models Based on Convolutional Neural Networks

Fatih Uysal <sup>1\*</sup>, Fırat Hardalaç <sup>1</sup>, Ozan Peker <sup>1</sup>, Tolga Tolunay <sup>2</sup> and Nil Tokgöz <sup>3</sup>

<sup>1</sup> Department of Electrical and Electronics Engineering, Faculty of Engineering, Gazi University, TR 06570 Ankara, Republic of Turkey; uysal@gazi.edu.tr; firat@gazi.edu.tr; ozan.peker@gazi.edu.tr

<sup>2</sup> Department of Orthopaedics and Traumatology, Faculty of Medicine, Gazi University, TR 06570 Ankara, Republic of Turkey; tolgatolunay@gazi.edu.tr

<sup>3</sup> Department of Radiology, Faculty of Medicine, Gazi University, TR 06570 Ankara, Republic of Turkey; nil.tokgoz@gazi.edu.tr

\* Correspondence: uysal@gazi.edu.tr; Tel.: +90 534 022 61 28

**Abstract:** Fractures occur in the shoulder area, which has a wider range of motion than other joints in the body, due to various reasons. To diagnose these fractures the data gathered from X-radiation (X-ray), magnetic resonance imaging (MRI) or computed tomography (CT) are used. In this study, it is aimed to help physicians by classifying the shoulder images taken from X-Ray devices as fracture / non-fracture with artificial intelligence. For this purpose, the performances of 26 deep learning-based pretrained models in the detection of shoulder fractures were evaluated on the musculoskeletal radiographs (MURA) dataset, and 2 ensemble learning models (EL1, EL2) were developed. The pretrained models used are ResNet, ResNeXt, DenseNet, VGG, Inception, MobileNet and their versions with Spinal fully connected (Spinal FC). In EL1 and EL2 models developed using pretrained models with the highest test performance, test accuracy was 0.8455, 0.8472; Cohens kappa 0.6907, 0.6942; the area under the receiver operating characteristic (ROC) curve (AUC) 0.8862, 0.8695 values were obtained for the fracture class. As a result of 28 different classifications in total, the highest test accuracy and Cohen kappa value were obtained in the EL2 model, and the highest AUC value was obtained in the EL1 model.

**Keywords:** biomedical image classification; bone fractures; deep learning; ensemble learning; shoulder; transfer learning; X-ray

---

## 1. Introduction

Having a wider and more varied range of movement than the other joints in the body, the shoulder has a flexible structure. The fractures in the shoulder may result from incidents such as dislocation of the shoulder, engaging in contact sports and motor vehicle accidents, etc. The shoulder bone mainly consists of three different bones. These are as follows; The upper arm bone named 'humerus', the shoulder blade named 'scapula' and the collarbone named 'clavicle'. Figure-1 shows the anatomic structure of the shoulder bone. The image in this figure was taken from the MURA dataset used in this study, and the markings thereon were placed by the physicians at Gazi University. As observed in Figure-1; the upper end of the humerus has a ball-like shape that connects with the scapula, called the glenoid. The types of shoulder fractures vary depending on age. While most fractures in children occur in the clavicle bone, the most common fracture in adults occur on the top part of the humerus, i.e. the proximal humerus. The types of shoulder bone

fractures are divided into three categories in general. These are as follows; Clavicle fractures, which are the most common shoulder fracture, frequently the result of a fall; Scapula fractures, which rarely occur, usually resulting fractures, which occur as cracks in the upper part of the arm in individuals over 65 years of age. The images from X-ray devices are primarily used for imaging of the shoulder bone for diagnosis and treatment of such fractures, while MRI or CT devices may also be used when required [1].

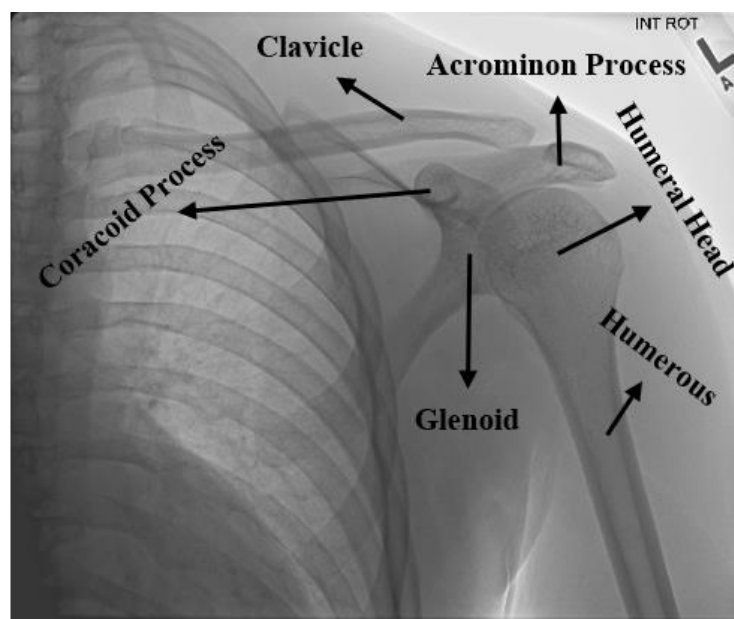


**Figure 1.** The anatomy of shoulder bone.

## 2. Related Works

Within the scope of this study; the classification of X-ray images of shoulder fractures in the MURA dataset was carried out into the categories of ‘fracture’ and ‘non-fracture’ by using built CNN-based deep learning models, new models thereof adapted to Spinal-Net and models developed based on ensemble learning. Therefore; two main topics have been taken into account while examining the literature regarding the study. Upon examination of the studies conducted thus far, these topics are as follows;

- What the studies conducted using the MURA dataset are, and why this dataset is preferred in this study,
- What kinds of studies have been conducted on classification of the shoulder bone images, and what kind of innovations may be set forth based on efficiency of deep learning models used in the classification procedures carried out within the scope of this study.

### 2.1. Studies Conducted Using MURA Dataset

MURA dataset was first introduced to the literature in a paper published in Open-Review platform, announced in the conference on “Medical Imaging with Deep Learning” held in Amsterdam in 2018. Following this publication, this dataset was made publicly available for academic studies within the scope of a competition called “Bone X-Ray Deep Learning Competition” by the Machine Learning group of the Stanford University. Being one of the largest public radiographic image datasets, MURA contains a total of 40,561 X-ray images with png format for the following parts of the body, labelled as either normal or abnormal (fracture); elbow, finger, forearm, hand, humerus, shoulder and wrist.

Within the scope of this classification study conducted by Rajpurkar et al. using DenseNet-169 on this dataset, the AUC score representing the area under the overall Receiver Operator Characteristics (ROC) curve was achieved as 0.929, and the overall Cohen's Kappa score was achieved as 0.705 [2]. Following this first study in which this dataset was introduced to the literature, there have been various studies that have been conducted and published using all or a part of the dataset. These studies are as follows: An average precision (AP) value of 62.04% was achieved in the fracture detection procedure using the proposed deep CNN model after the fractures were marked by the physicians on the arm X-ray images in the MURA dataset by Guan et al. [3]. The following classification accuracies were achieved by Galal et al. using a very small part of the elbow X-ray images in the MURA dataset (56 images for the train dataset, 24 images for the test); 97% with the support vector machine (SVM), 91.6% with random forest (RF), and 91.6% with naive bayes [4]. The classification by Liang and Gu with multi-scale CNN and graph convolution network (GCN) they proposed using the entire MURA dataset achieved a result of an overall Cohen's Kappa score of 0.836. [5]. The overall Cohen's Kappa score achieved by Saif et al. within the scope of classification performed using the whole MURA dataset with the proposed capsule network architecture was 0.80115 [6]. Within the scope of the classification carried out by Cheng et al. using the dataset containing hip bone images and the whole MURA dataset, the highest accuracy achieved was 86.53% for humerus images with the proposed adversarial policy gradient augmentation (APGA) [7]. The highest accuracy achieved in the classification performed by Pelka et al. using the whole MURA dataset was 79.85% with the InceptionV3 model [8]. The AUC score was achieved as 0.88 in the classification carried out by Varma et al. on Lower Extremity Radiographs Dataset (LERA) containing data for foot, knee, ankle and hip for ImageNet and DenseNet161 model pre-trained with MURA [9]. In the classification performed by Harini et al. on images of finger, wrist and shoulder in MURA dataset using five different CNN-based built deep learning method, the highest accuracy was achieved as 56.30% on the wrist data with DenseNet169 [10]. The overall accuracy achieved for MURA with the proposed iterative fusion CNN (IFCNN) method is 73.4% within the scope of classification carried out by Fang et al. using the optical coherence tomography (OCT) dataset and the entire MURA dataset [11]. The overall Cohen's Kappa score achieved was 0.717 with the proposed deep CNN-based ensemble model in the classification carried out by Mondol et al. on elbow, finger, humerus and wrist data in the MURA dataset [12]. In the type classification performed by Pradhan et al. using the whole MURA dataset, 91.37% accuracy was achieved with the proposed deep CNN model [13]. Within the scope of the classification carried out by Shao and Wang using the entire MURA dataset, a two-stage method was developed and the highest accuracy achieved was in humerus images with 88.5% for the SENet154 model, while the highest accuracy for the DenseNet201 model was achieved on again humerus images with 90.94% [14].

Although there are many different publicly available datasets on bone fracture in addition to MURA dataset in the literature, the main reason for using only this dataset in this study is that MURA is one of the largest datasets for both groups of normal (negative, non-fracture) and abnormal (positive, fracture) compared to the other public datasets. It is observed upon examination of the studies conducted via this dataset that classification and / or fracture detection procedures are carried out using the dataset in whole or in part. Only the X-ray images for shoulder bone in the MURA dataset were used in this study. The reason why only this type of dataset was used for classification despite the availability of 7 different type of datasets and the reason why such dataset is for the shoulder data is that the shoulder dataset is proximately the most balanced type in terms of distribution of the amount of data provided for both training and validation. Another reason for classification for a single type only is to be able to develop the most optimum model for fracture

and non-fracture images on this type using / developing as many different deep learning models as possible.

## 2.2. Classification Studies Carried Out on the Shoulder Bone

While some of the studies mentioned under the previous title with the MURA dataset include classification of shoulder bone images, there are also studies in the literature on classification of the shoulder bone exclusively. These studies are as follows: As the result of the classification carried out by Chung et al. with ResNet152 model on a total of 1376 abnormal CT images, including 1891 normal and four different type of proximal humeral fractures, a 96% accuracy was achieved [15]. Within the scope of the CNN model proposed by Sezers using a total of 219 shoulder MR images, a classification was made in three different groups as normal, edematous and Hill-Sachs lesions with 98.43% accuracy [16]. The highest accuracy achieved in the classification carried out by Urban et al. on 597 X-ray images of shoulders with implants was 80.4% in the NASNet model pre-trained with ImageNet [17]. Within the scope of the classification performed by Sezer et al. using a total of 219 shoulder MR images grouped as 91 edematous, 49 Hill-Sachs lesions and 79 normal, 88% success rate was achieved with kernel-based SVM and 94% success was achieved with extreme learning machines [18]. 94.74% accuracy was achieved with the proposed CapsNet model in the classification performed by Sezers on a total of 1006 shoulder MR images, grouped as 316 normal, 311 degenerated and 379 torn [19].

It is observed upon examination of the recent classification studies on shoulder bone in the literature that the normal and abnormal (fracture, edematous, Hill-Sachs lesion, degenerated, torn) images obtained from CT, MRI or X-ray devices are classified by not only the traditional machine learning methods such as SVM but also by deep learning-based methods such as ResNet, NasNet, CapsNet. In this study, the classification was performed on shoulder bone X-ray normal / abnormal (fracture) images in the MURA dataset. In performance thereof, as a practice different from the literature, built CNN-based deep learning models (ResNet, ResNeXt, DenseNet, VGG, InceptionV3 and MobileNetV2) with varied structure and number of layers were used by transfer learning with pretrained ImageNet by also adding SpinalNet to the classification layers. Based on the results of classification achieved by the procedures performed herein, another classification was performed with ensemble learning. The main reason for applying transfer learning on built CNN models, adding SpinalNet as well as applying ensemble learning is to contribute to the efficiency of deep learning models proposed in classification of shoulder bone X-ray images.

The title of 'methods', constituting the 3rd part of the study, discusses CNN-based built deep learning models such as ResNet, DenseNet, VGG, InceptionV3 etc. used in classification as well as their adaptations with SpinalFC and proposed ensemble learning models. Under the 4th part titled 'the experiments', the open source dataset including the shoulder bone X-ray images, data augmentation and data pre-processing procedures applied on this dataset as well as a table containing the accuracy, recall, f1-score and Cohen's Kappa scores achieved by classification models, and the results of classification including confusion matrix and ROC curves and AUC scores are explained. The 'conclusion' and 'future work' titles constituting the final part of the study provides information on interpretation of the results achieved by classification models, the contribution of this study to the literature and improvements that can be applied in future work.

## 3. Methods

A number of different deep learning-based methods have been used and developed to classify X-ray images of the shoulder bone with png format and 3-channels as normal

and abnormal within the scope of the study. Firstly, classification was performed with ResNet (34,50,101,152), ResNeXt (50,101), DenseNet (169,201), VGG (13,16,19), InceptionV3 and MobileNetV2, which are CNN-based deep learning models with different structures and layers available for use in the literature. Subsequently, new classification networks were established by replacement of the classification layer of each model used herein with the SpinalNet FC layer. Based on the results obtained herein, new ensemble learning models specific to this study were developed in order to further increase the classification accuracy. Built deep learning models, newly developed models with SpinalNet and details of the ensemble learning models used for classification have been described in the following subtitles.

### 3.1. Classification Models Based on CNNs for Shoulder Bone X-Ray Images

The CNN-based deep learning models currently available in the literature were used in classification of the X-ray images of the shoulder bone in the first place. In training of the models, training was firstly carried out with the data in the training section of the dataset without pretraining, i.e. with random weight as the initial weight. However, the required level could not be reached in the training of the network and at the end of the classification by this application. Therefore the transfer learning method has been applied.

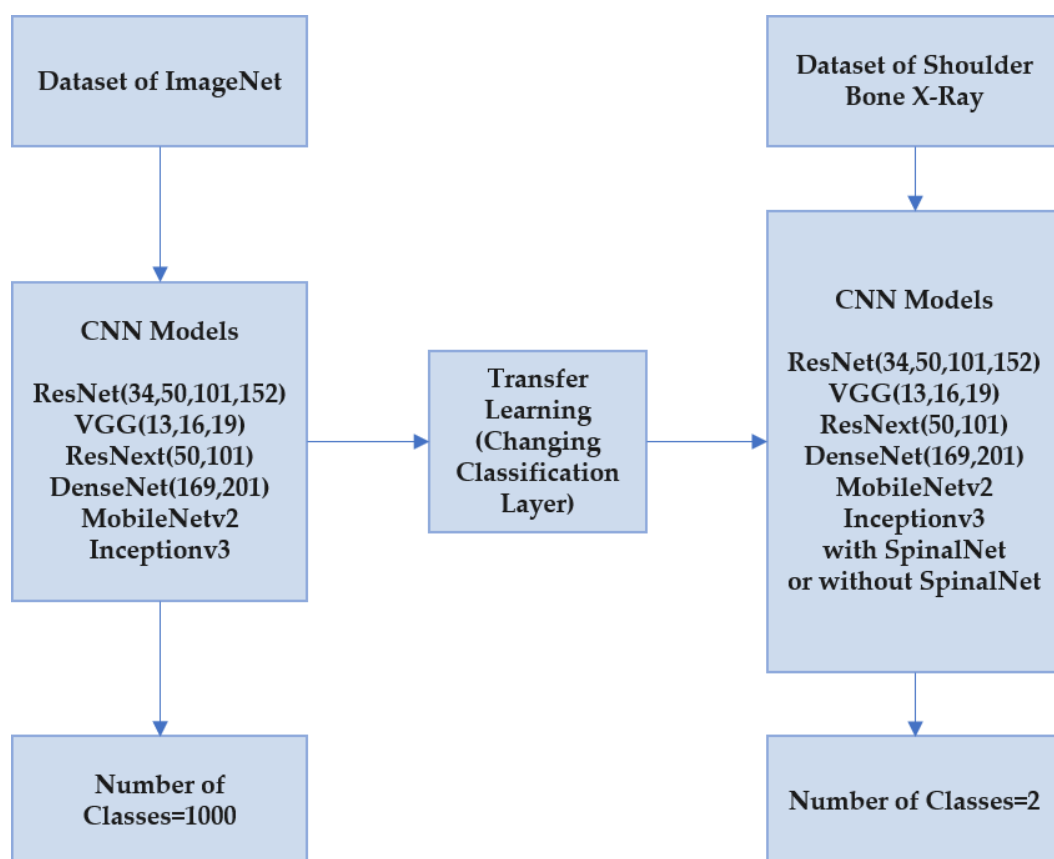


**Figure 2.** StandartFC/SpinalFC version CNN based deep learning methods subject to transfer learning.

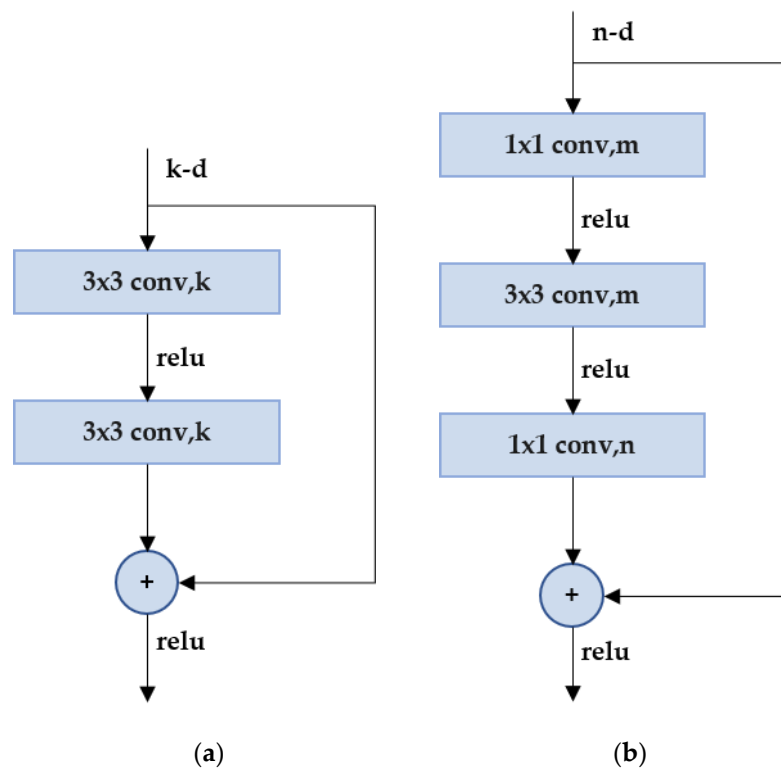
Within the scope of this transfer learning method, the version of each available deep learning model pre-trained with ImageNet data, i.e. the existing weights in the pretrained models, were used in the first place. ImageNet is a dataset and benchmark that contains millions of images and hundreds of object categories, on which mainly the procedures of

image classification, single-object localization and object detection are performed [20]. Shoulder bone X-ray images dataset used in this study was used for input of the deep learning models, which are specified in Figure 2 and trained with ImageNet data. The structure comprised of 1000 classes in the last layer of these models has been made into two classes in order to classify bone images specific to our study as normal and abnormal. Following the abovementioned procedures, classification was carried out by training the network with the shoulder dataset. Moreover, the last layer of these 13 built deep learning models were fine-tuned with SpinalNet / SpinalFC within the scope of the study; and with the newly acquired models, shoulder bone X-ray images were trained and classified.

The ResNet, ResNeXt, DenseNet, VGG, InceptionV3 and MobileNetV2 deep learning models currently available in the literature, which can be used in the classification, and their versions with different layer numbers are some of the models used in classification of the shoulder bone X-ray images within the scope of this study. The method-based details required regarding these models and SpinalNet within the scope of this study are described under the following subtitles.

### 3.1.1. ResNet

Deep residual networks as ResNet is a CNN-based deep learning model including more than one building blocks of residual learning depending on the number of layers [21]. In part (a) of the following figure, there are  $k$  number of building blocks with  $3 \times 3$  conv for ResNet34, and in part (b), there are  $m$  number of building blocks with  $1 \times 1$  and  $3 \times 3$  conv, and  $n$  number of building blocks with  $1 \times 1$  conv for ResNet50,101,152, respectively.



**Figure 3.** ResNet building block. (a) BB-I,  $k$ ; (b) BB-II,  $m$ ,  $n$ .

In this study, 4 ResNet models with 34, 50, 101 and 152 layers, respectively, were used in classification. The structure of these ResNet-based models used and adapted is as follows:

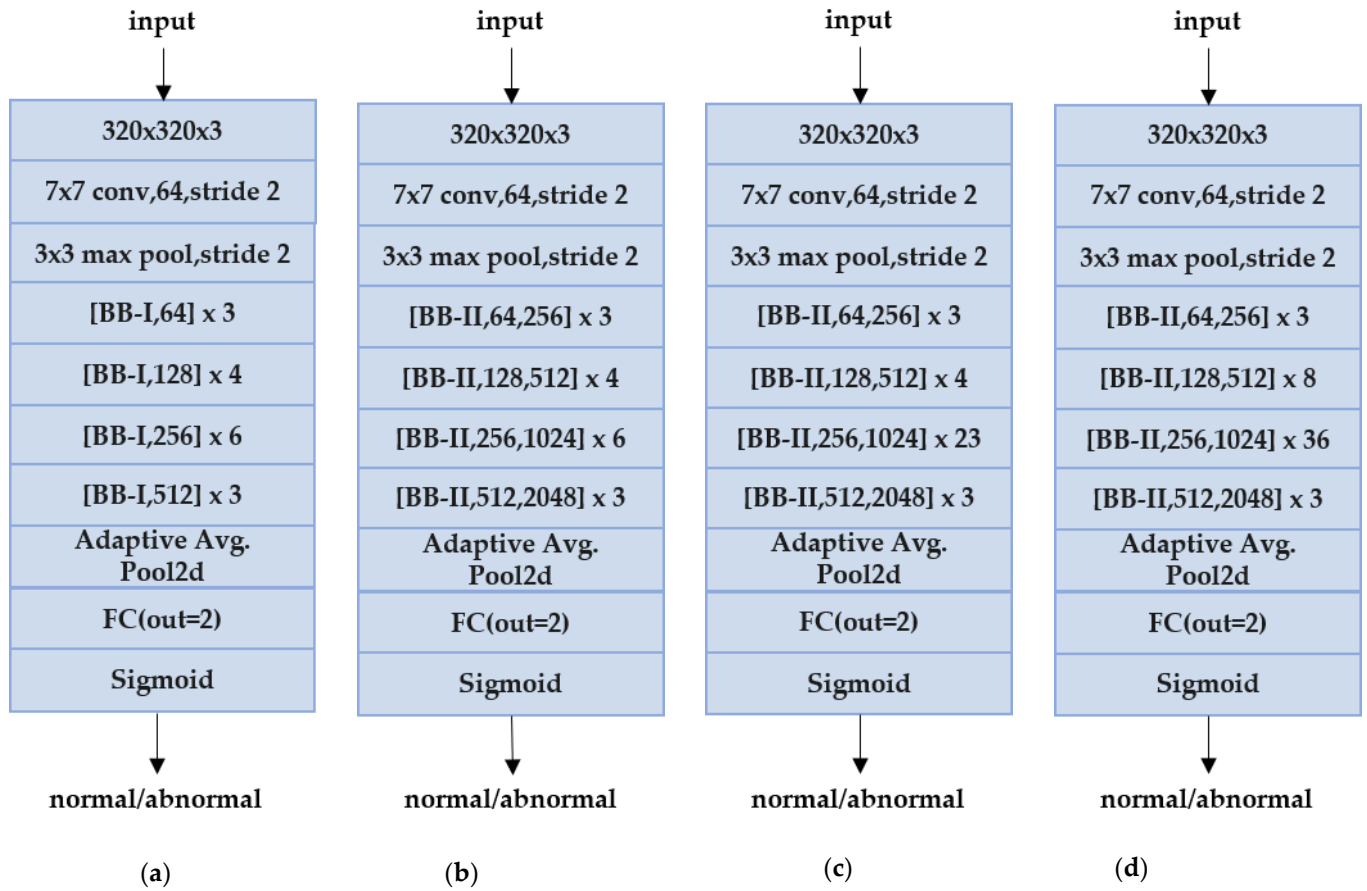


**Figure 4.** The structure of the adapted ResNet-based models. (a) ResNet34; (b) ResNet50; (c) ResNet101; (d) ResNet152.

### 3.1.2. ResNeXt

ResNeXt is a deep learning model for deep neural networks that reduces the number of parameters in ResNet. With this model, cardinality, which is an additional dimension for the width and depth of ResNet, defining the size of the set of transformations, is used [22]. The structure of the ResNext block is presented below. In this structure, there is a block structure with a cardinality value of 32, with  $r$  number of 1x1 and 3x3 conv and  $s$  number of 1x1 conv, respectively.

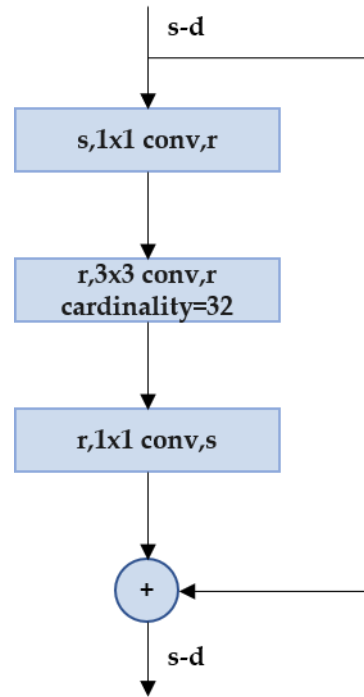


**Figure 5.** ResNeXt building block (BB-III,  $r$ ,  $s$ ,  $C=32$ ).

2 ResNeXt models with 50 and 101 layers, respectively, were used in classification in this study. The structure of these ResNeXt-based models used and adapted is as follows:

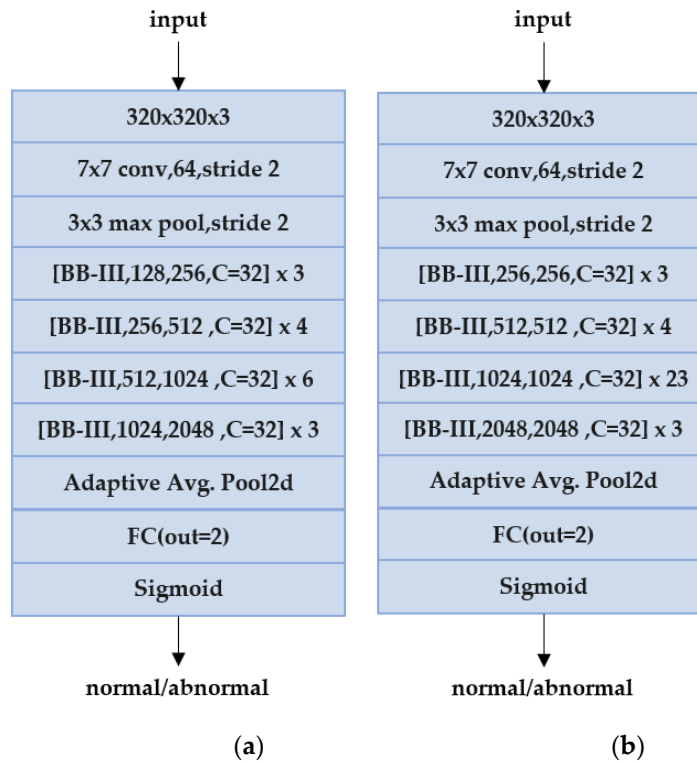


**Figure 6.** The structure of the adapted ResNeXt-based models. (a) ResNeXt50 (32x4d); (b) ResNeXt101 (32x8d).



### 3.1.3. DenseNet

In dense convolutional neural networks known as DenseNet, each layer affects every other layer in a feed-forward fashion [23]. The structure of the dense block is as follows. This dense block consists of a total of 5 layers. The first 4 layers have a dense layer, and the last layer has a transition layer. If the growth rate value is ( $k$ ) for each layer, it is 4 for this dense block. On the transition layer, there is a  $2 \times 2$  average pool with  $1 \times 1$  conv and stride 2. On the dense layer, there are  $1 \times 1$  and  $3 \times 3$  convs with stride 1.

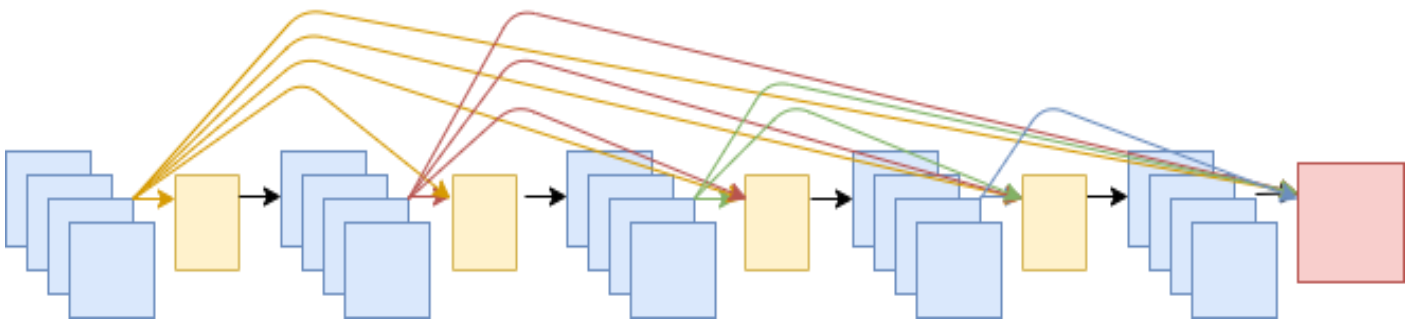


**Figure 7.** DenseNet block. (The yellow coloured layers are BatchNorm-ReLu-Conv, and the red colored layer is the transition layer.).

Within the scope of this study, 2 DenseNet models with 169 and 201 layers, respectively, and a growth rate ( $k$ ) of 32 were used in classification. The structure of these DenseNet-based models used and adapted is as follows:

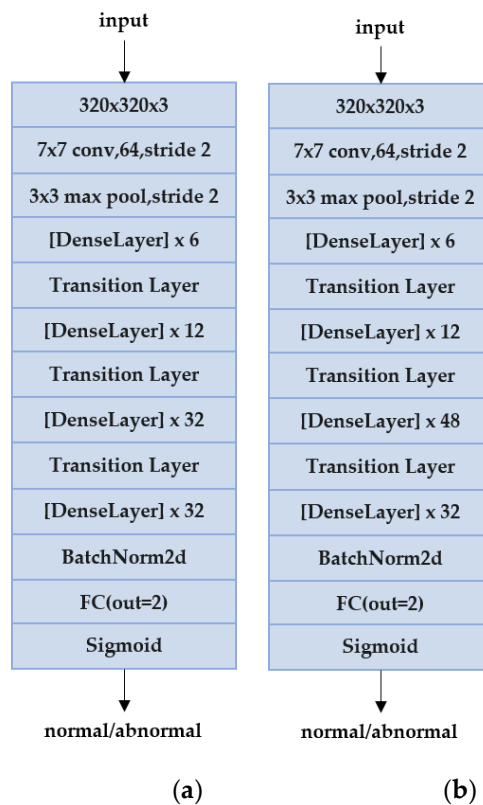


**Figure 8.** The structure of the adapted DenseNet-based models. (a) DenseNet169; (b) DenseNet201.

### 3.1.4. VGG

VGG is a CNN-based deep learning model with very small (3x3) convolution filters [24]. In this study, 3 VGG models with 13, 16 and 19 layers, respectively, were used for the classification procedure. The structure of conv blocks comprised of combination of 2, 3 or 4 consecutive 3x3 conv (with k, m or n filters) layers and these VGG based models, which are used / adapted from combination thereof, is as follows:

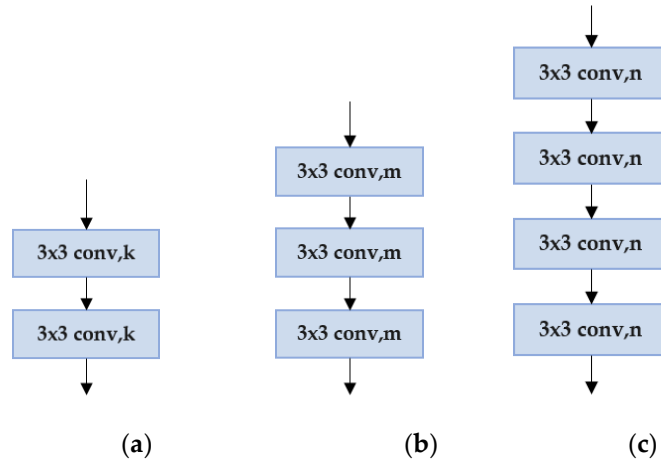


**Figure 9.** The conv blocks of 2, 3 and 4 comprised of 3x3 conv layers (CB-I, II, III, respectively). (a) CB-I, k; (b) CB-II, m; (c) CB-III, n.

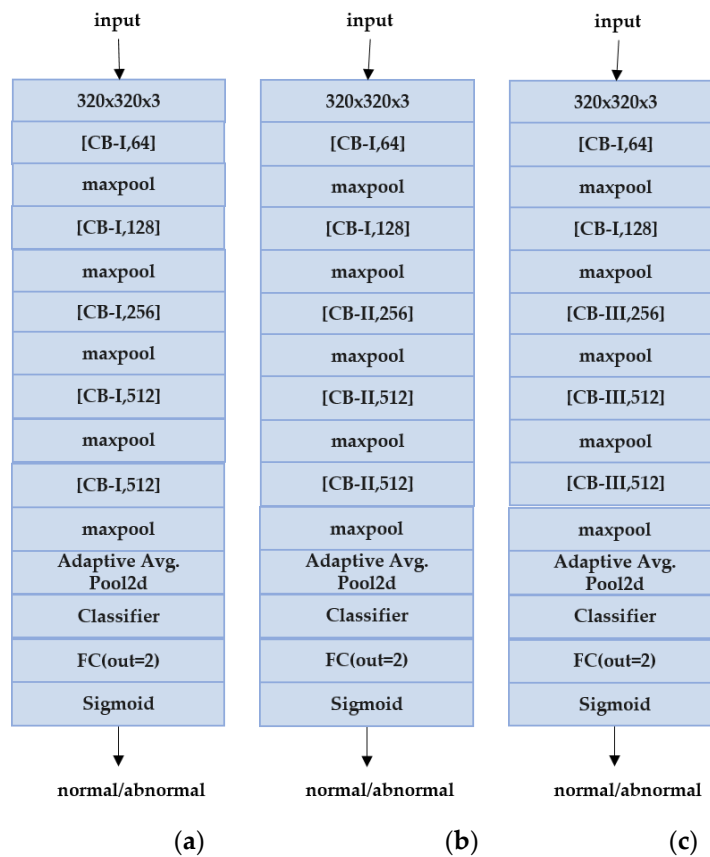


**Figure 10.** The structure of the adapted VGG-based models. (a) VGG13; (b) VGG16; (c) VGG19.

### 3.1.5. InceptionV3

InceptionV3 is a CNN-based deep learning model that includes convolution factorization, which is called the inception module [25]. The structure of the inception module is as follows.

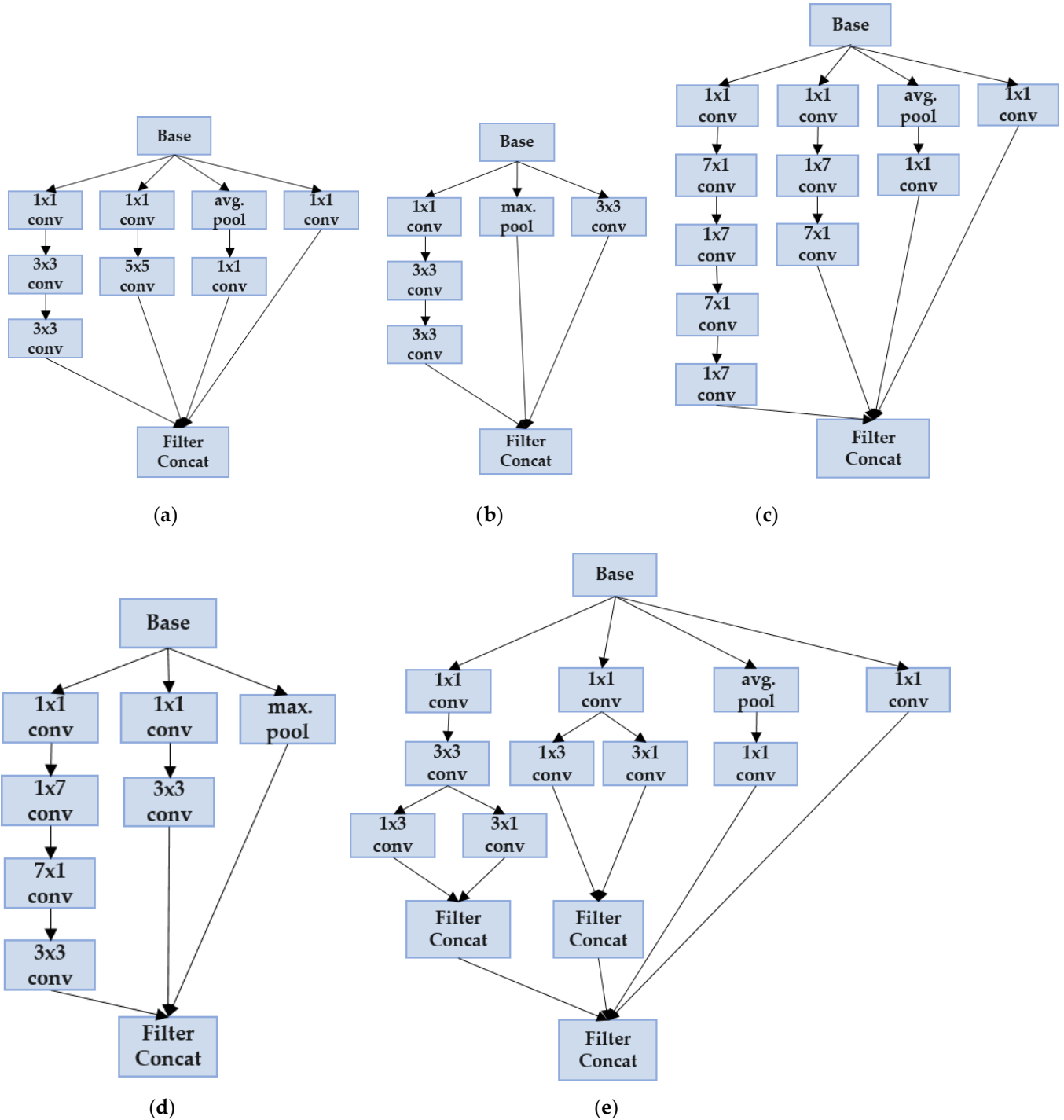


**Figure 11.** The inception blocks containing convolution factorization (IB-A, B, C, D, E). (a) IB-A; (b) IB-B; (c) IB-C; (d) IB-D; (e) IB-E.

In this study, InceptionV3 model was used in classification. The structure of this Inception V3-based model used and adapted is as follows:

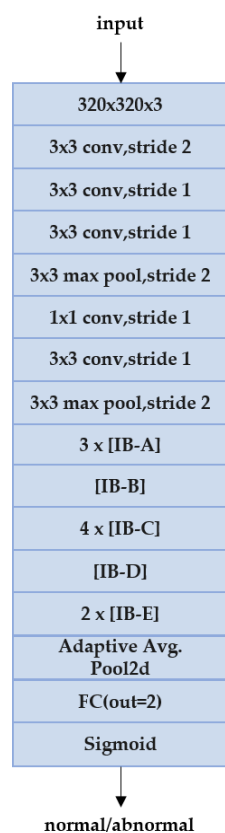


**Figure 12.** The structure of adapted InceptionV3-based model.

### 3.1.6. MobileNetV2

MobileNetV2 is a deep learning model that includes residual bottleneck layers [26]. The structure of the convolution block of this model is as follows

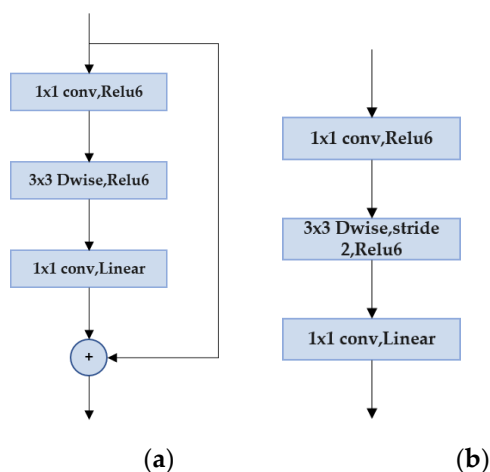


**Figure 13.** MobileNet bottleneck blocks for stride = 1 and stride = 2, respectively (MB-I, II). (a) MB-I; (b) MB-II.

MobileNetV2 model was used in classification within the scope of this study. The structure of this MobileNetV2-based model used and adapted in this study, which contains a total of 17 MobileNet bottleneck blocks, comprised of 13 bottlenecks with a stride value of 1, and 4 bottlenecks with a stride value of 2, is as follows:



**Figure 14.** The structure of adapted MobileNetV2-based model.

### 3.2. SpinalNet

In SpinalNet, the structure of hidden layers is different from a normal neural network model. In a neural network, the hidden layers receive inputs in the first layer and then transfer the intermediate outputs to the next layer. However, the hidden layer in SpinalNet enables the previous layer to receive a certain part of its inputs and outputs. Therefore, the number of incoming weights in the hidden layer is lower than normal neural networks [27]. The following figure shows the basic structure of the traditional and spinal hidden layers.

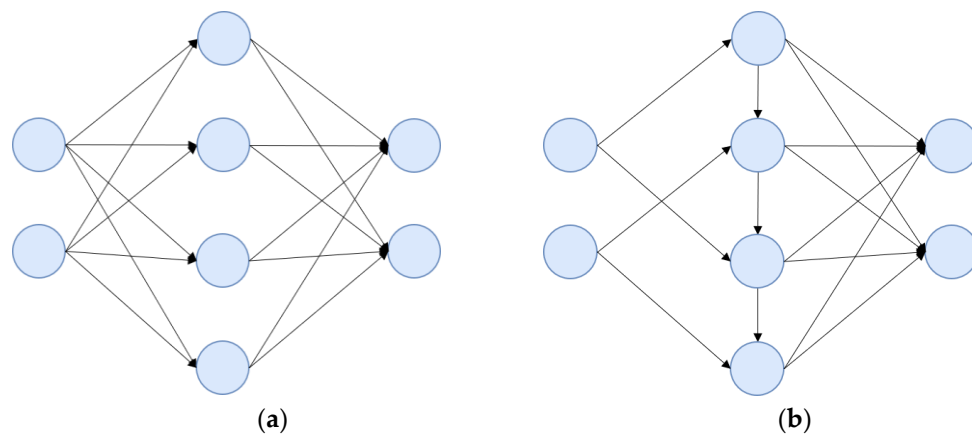


**Figure 15.** Basic structures of traditional (standard) FC and Spinal FC layers. (a) Standart FC; (b) Spinal FC.

Within the scope of this study, the classification layer of 13 CNN models based on the ResNet, ResNeXt, DenseNet, VGG, InceptionV3 and MobileNetV2, which were above-mentioned in the previous section and used in classification, was adapted with SpinalNet / SpinalFC, and a classification was also carried out with SpinalFC versions of these models. This allowed observation of the effect of SpinalNet on classification of the shoulder bone X-ray images. The details regarding such effect are described in the ‘experiments’ section of the study. Moreover, the layer widths in Spinal FC of each classification model are as follows.

**Table 1.** Layer with values of SpinalFCs used in classification models.

Models	SpinalFC layer with	Models	SpinalFC layer with
ResNet34	256	ResNeXt50	20
ResNet50	128	ResNeXt101	128
ResNet101,152	1024	DenseNet169, 201	240
VGG13	256	MobileNetV2	320
VGG16,19	512	InceptionV3	20

### 3.3. Proposed Classification Models Based on EL for Shoulder Bone X-Ray Images

Two ensemble models were established to further increase the accuracy of classification by examining the classification results of shoulder bone X-ray images performed with the CNN-based models and their SpinalNet versions used within the scope of the study and aforementioned in the previous sections. While choosing the sub-models required for ensemble learning, the accuracy rates in classification results of each model, the confusion matrix scores, and the (normal / abnormal) AUC scores for each class were taken into consideration. The details of these two ensemble-based classification models are explained under the subtitles.

#### 3.3.1. EL1 (ResNeXt50 with Spinal FC, DenseNet169 with Standard FC, DenseNet201 with Spinal FC)

EL1 (Ensemble learning-1) model was developed using the combination of the networks of ResNeXt50 with spinal FC, DenseNet169 with standard FC and DenseNet201 with spinal FC. The schematic diagram of the developed model is as follows.

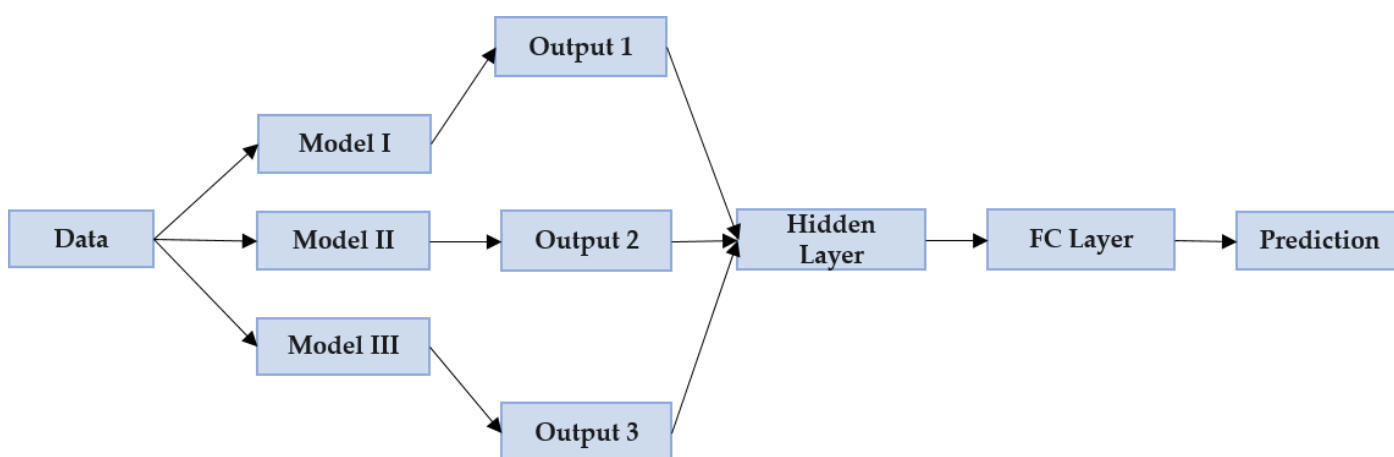


**Figure 16.** Proposed EL1 classification model.

It is observed upon examination of the figure above on the EL1 model proposed for classification of shoulder bone X-ray images as normal / abnormal (fracture) that three different CNN-based models are used. The “data” specified in this figure represents the entire dataset of shoulder bone X-ray images, “model I” is ResNeXt50 model with SpinalNet FC, “model II” is DenseNet169 model with Standart FC layer, “model III” DenseNet201 model with SpinalNet FC, “output I-II-III” are the output of these three models and the “prediction” last part are the normal/abnormal (fracture) class types. In selection of the three models specified in this ensemble model, the parameters in the training outputs of the 26 CNN models presented in the previous title were taken into consideration. These parameters can be stated as Cohen’s Kappa score, AUC, and test accuracy. Detailed steps of procedure for the proposed EL1 ensemble model are as follows:

- Step1: First of all, the last layers of 3 pre-trained sub-models in the EL1 ensemble model, are adjusted as the Identity layer.
- Step2: After this process, the final layer with 80 outputs for ResNext50 with spinal FC, 1664 for DenseNet169 with standard FC, 960 for DenseNet201 with spinal FC are achieved.
- Step3: Then these outputs are combined to form a single linear layer and a hidden layer with 2704 outputs is achieved.
- Step4: This hidden layer is finally connected to the classifying layer connected to the sigmoid activation function, the output of which is 2.
- Step5: The network established as the result of these procedures is re-trained, providing results.

3.3.2. EL2 (ResNet34 with Spinal FC, DenseNet169 with Standart FC, DenseNet201 with Spinal FC, ResNext50 with Spinal FC)

EL2 (Ensemble learning-2) model was developed using the combination of ResNet34 with spinal FC, DenseNet169 with standard FC, DenseNet201 with spinal FC and an sub-ensemble model. Schematic diagram of the developed model is provided in Figure 17. It is observed upon examination of the figure that the EL2 model, differently from the EL1 model, consists of 3 single models and 1 sub-ensemble model and has a different structure. The “X-Ray Images” specified in the Figure refers to the dataset containing shoulder bone images, “Model I” to ResNet34 model with spinal FC, “Model II” to DenseNet201 model with spinal FC, “Model III” to the sub-ensemble model, “Model IV” to DenseNet169 model with standard FC and “Prediction I-II-III-IV” refers to the outputs of the classification performed with these 4 models. Detailed parts of procedure for the proposed EL2 ensemble model are as follows:

- Part1: In the “Input” section, there is a shoulder X-ray image dataset that has been subjected to certain image processing techniques.
- Part2: In the “Classification Network” section, the models that establish our ensemble model are defined. There are 3 single sub-models and an sub-ensemble model that constitute our ensemble model therein. Our sub-ensemble model is an architecture trained by connecting the predicted outputs of ResNet34 with Spinal FC, DenseNet201, ResNeXt50 and DenseNet169 with Standard FC to a linear layer with 8 inputs and 2 outputs. The evaluation of 26 models as single was effective in selection of these four models
- Part3: In the “Predictions” section, there are the outputs of normal / abnormal (fracture) class types achieved as the result of the classification performed in the previous section.
- Part4: In the “Main Check” section, there is the main check mechanism that plays a role in determination of the class of the input image. Therein, the Model I and Model II suggests classifying the input image as abnormal in the final classification, while

Model III and Model IV suggests classifying the input image as normal in the final classification. In cases where suggestions are not available, the classification is carried out with the sub-ensemble model. In selection of the referred models for each class, Confusion Matrix and Recall parameters previously obtained for 26 CNN models were taken into consideration.

- Part5: In the "Sub Check" section, there is a supplementary check mechanism under the main check mechanism. The aim here is to use the classification result of another model (Model IV for class1 (abnormal), Model II for class0 (normal)) other than the two models referred to at the main check section, as a supplementary for the final classification process.
- Part6: In the "Final Prediction" section, the final output determined as the result of the check mechanisms is achieved.

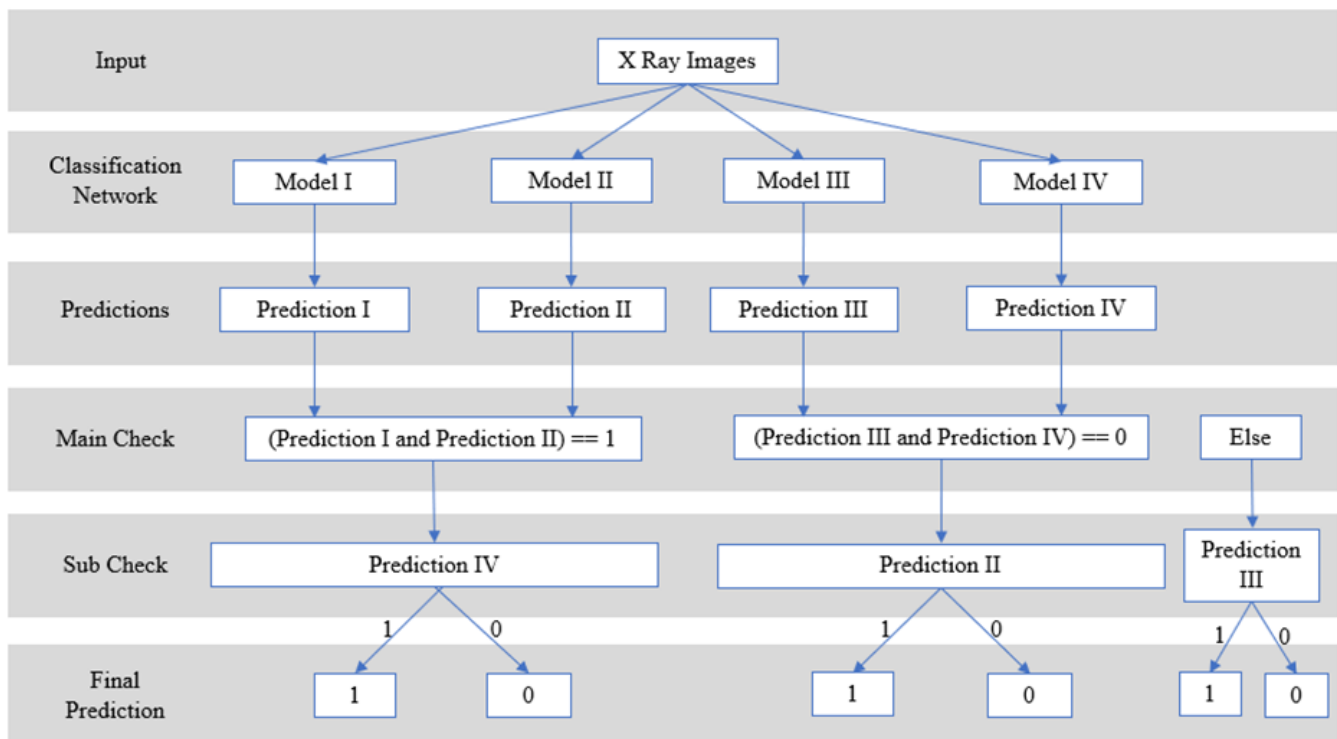


**Figure 17.** Proposed EL2 classification model.

The structure of the EL2 model is explained in algorithm 1.

**Algorithm 1 EL2**

**Input:**Shoulder bone X-ray images

Dataset=test\_dataset

**Process:**

```

for image in test_dataset:
    pred_1=Model_I(image)
    pred_2=Model_II(image)
    pred_3=Model_III(image)
    pred_4=Model_IV(image)
    if (pred_1 and pred_2==1):
        if pred_4==1:
            final_pred=1:
        if pred_4==0:
            final_pred=0:
  
```



---

```

elif( pred_3 and pred_4==0):
    if pred_2==1:
        final_pred=1:
    if pred_2==0:
        final_pred=0:
else:
    final_pred=pred_3
Output:final_pred

```

---

#### 4. Experiments

In this study where shoulder bone X-ray images are classified as fracture, CNN-based deep learning (DL) models have been used. In this study in which X-ray images of the shoulder bone in the open source MURA dataset were used, data pre-processing / augmentation was performed as a first step. Following this process, classification was carried out using 13 different CNN models, SpinalNet versions of these models and 2 ensemble learning model. The proposed classification models for normal / abnormal (fracture) shoulder bone X-ray images are as follows.

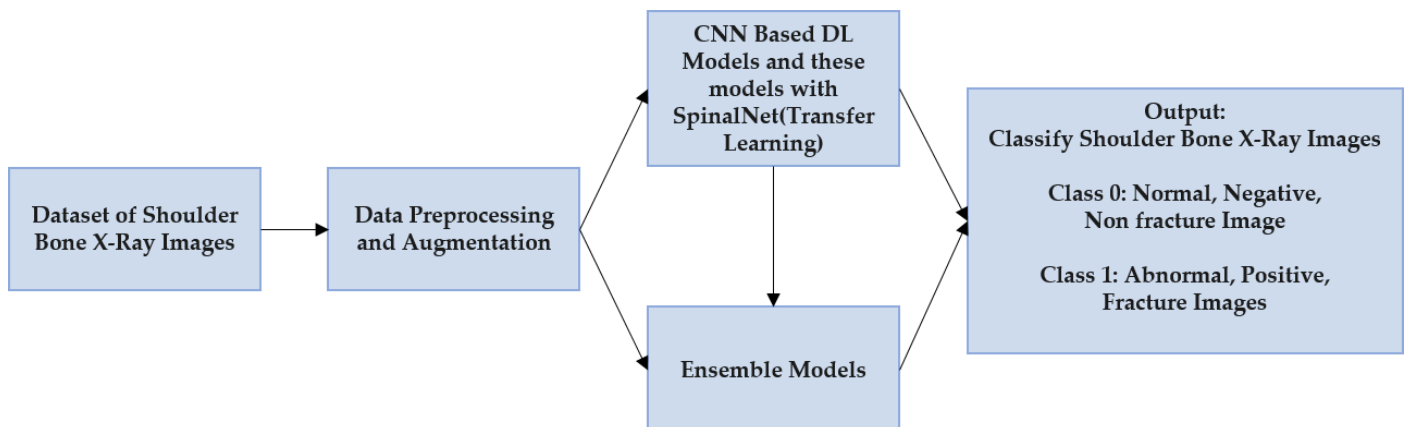


**Figure 18.** Proposed classification models of shoulder bone X-ray images.

##### 4.1. Dataset of Shoulder Bone X-Ray Images

An open source dataset named MURA (Musculoskeletal Radiographs) published by the Stanford University Machine Learning group was used within the scope of the study. This dataset is one of the largest bone X-ray image datasets published among the open radiography datasets. It is a dataset containing 7 different types of bone X-ray images including finger, elbow, wrist, hand, forearm, humerus and shoulder [2]. In this study, solely the shoulder bone X-ray images within the MURA dataset were used. The main reason for choosing the shoulder dataset is that it is proximately the most balanced type in the MURA dataset in terms of distribution of the amount of data provided for both training and validation. Such balanced distribution is presented in figure 19. Although the MURA dataset is an open source dataset, it is concluded upon detailed examination of the dataset that only the training and validation datasets are publicly available. The classification models used in the first study conducted with MURA dataset and in the studies conducted within the scope of the competition held regarding the MURA were tested using test data that are not publicly available. Due to confidential nature of the test data and inability to conduct test with these data as the competition was completed, the validation data was used as the test data within the scope of this study.

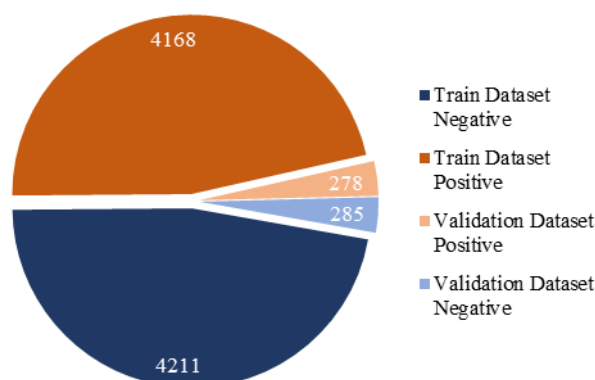


**Figure 19.** Shoulder bone X-ray dataset.

These images, which initially had different resolutions and 3 channels, were first pre-processed and then converted into 320x320x3 pixels before being used for the deep learning model. The reason why the image sizes were converted to 320x320x3 is that it is the most compatible resolution in the similar studies using this dataset. The data formats are png, and no alterations were made in terms of the format type. The image type of the shoulder bone X-ray images, the number of training images, the number of test images, the original and new image sizes are provided in the table below.

**Table 2.** Details of the shoulder bone X-ray images used in the study.

Shoulder bone X-ray images	Image types	Train dataset	Test dataset	Org. image size	New images size
<b>Class 0:</b>					
<b>Normal (Negative) bone X-ray images</b>	png, 3-ch.	4211	285	various	320x320x3
<b>Class 1:</b>					
<b>Abnormal (Positive) bone X-ray images</b>	png, 3-ch.	4168	278	various	320x320x3
<b>Total</b>	png, 3-ch.	8379	563	various	320x320x3

It is observed upon examination of the table above presenting information on shoulder bone X-ray images that the image sizes were originally different but later converted to 320x320x3 in size; all image formats are png; and the original quantity of images is 4211 in the training section and 285 in the test section for normal images, and 4168 in the training section and 278 in the test section for abnormal images.

#### 4.2. Data Augmentation for Shoulder Bone X-Ray Images

Since the results obtained in deep learning, particularly in classification studies, are very sensitive to the dataset and the increase in the amount of data in the training stage of the network has a positive effect on the training of the network, the quantity of shoulder

bone x-ray images in the MURA dataset used in this study were increased by data augmentation. For this procedure, new images were obtained by rotating the images to the right and left to a maximum of 10 degrees.

#### 4.3. Data Pre-processing for Shoulder Bone X-Ray Images

It is observed upon examination of the shoulder bone X-ray images of the MURA dataset used in the study that there are both noise and a dark background on these images, which may adversely affect the classification and / or fracture detection processes. Various pre-processing steps have been applied on the dataset in order to eliminate the abovementioned adverse effects as much as possible and to obtain more meaningful results in the classification process. These pre-processing steps are listed below.

- **Detection of the Corresponding Area:** Most of the X-ray images in the used dataset are insufficient in terms of semantic information contained compared to the image size. In order to eliminate such insufficiency, the images are first converted to gray-scale and then subjected to double thresholding and to the adaptive threshold value determined by using Otsu's thresholding value method. In the gray-scale images, the within-class variance value corresponding to all possible threshold values for the two colour classes assumed as background and foreground is calculated. The threshold value that makes this variance the smallest is the optimal threshold value. This method is known as Otsu's thresholding value method [28]. Subsequently, the edge in the thresholded image is determined using the edge detection methods. After this process, the original image is cropped based on the calculated values.
- **CLAHE Transformation:** As the next step of data pre-processing, the contrast-limited adaptive histogram equalization (CLAHE) transformation in the OpenCV library was used. Within the scope of the transformation used, the input image is divided into parts as determined by the user, with each part containing a histogram within itself. Then, the histogram of the part is adjusted based on the histogram cropping limit entered by the user, and finally, all parts are brought together to obtain a Clahe-transformed version of the input image [29,30]. New outputs are achieved by contrast equalization of the cropped images by CLAHE method.
- **Normalization and Standardization:** As the last step, the images are normalized and standardized using the image-net values.

An example of the shoulder bone X-ray images in their original version and in their version subjected to the abovementioned pre-processing steps for each class (normal / abnormal (fracture)) are provided in the following figure.

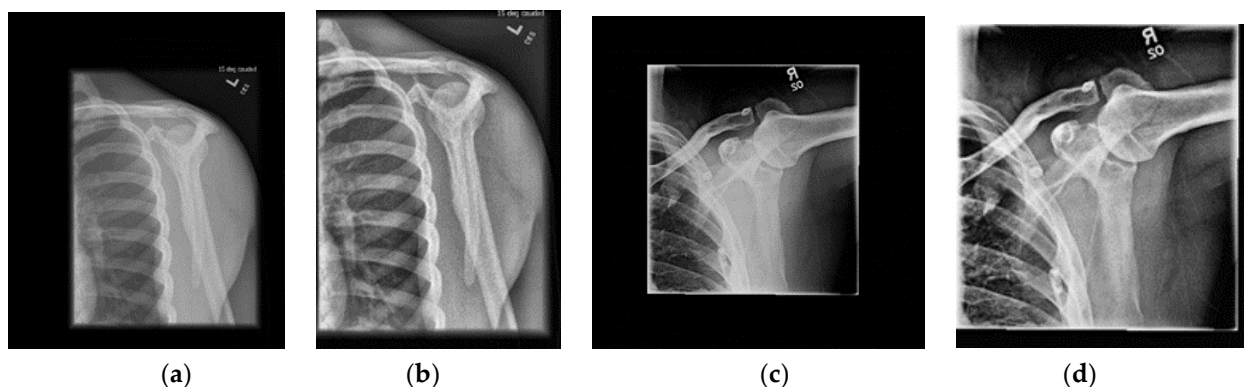


**Figure 20.** Original and pre-processed X-ray images of normal / abnormal (fractured) shoulder bone. (a) original normal; (b) pre-processed normal; (c) original abnormal (fracture); (d) pre-processed fracture.

In the figure above, the following are presented; in section a, original version of a normal (negative) shoulder bone X-ray image; in section b, the cropped and CLAHE pre-processed version of this normal image; in section c, the original version of an abnormal (positive, fractured) shoulder bone X-ray image; and in section d, the cropped and CLAHE pre-processed version of this abnormal image.

#### 4.4. Classification Results

Online servers were used as hardware in the process of classification of shoulder bone X-ray images as normal / abnormal (fracture) using deep learning methods within the scope of the study. The program codes of this study written using the PyTorch deep learning library are publicly available at <https://github.com/fatihuyul88/shoulder-c>. Learning rate 0.0001, epoch number 40, optimizer Adam, and loss function cross-entropy were used in all classification procedures performed with ResNet, ResNeXt, DenseNet, VGG, InceptionV3 and MobileNetV2 deep learning models. While the same learning rate, epoch number, optimizer, and loss function are used in the versions with SpinalNet of these models, SpinalFC is used in the classification layer. The learning rate value initially used with these models is not fixed, and it is decreased 10 times in every 10 epoch in order to increase network learning success. The same parameters are used in Ensemble learning models, as well.

##### 4.4.1. Evaluation Metrics

In order to evaluate the results obtained in classification problems accurately and completely, the following must be obtained; accuracy percentage, confusion matrix, precision, recall, f1-score from each classification model and ROC curves and AUC scores for each class. The accuracy percentage refers to what percentage of the test data has been correctly classified. Confusion matrix provides a table of the current status in the dataset and the number of correct and incorrect predictions of our classification model. This table contains true positive (TP), true negative (TN), false positive (FP), and false negative (FN) values. Precision refers to values predicted as positive. Recall is defined as true positive rate. F1-score is the harmonic mean of precision and recall values. Cohen's Kappa coefficient is a statistical method used to measure the reliability of agreement between two raters. The  $p_0$  value used in this calculation refers to the result of accuracy, and the  $p_e$  value refers to the probability of random agreement. The following tables contain information on what TP, TN, FP, FN, and confusion matrix refer to and how the accuracy, precision, recall, f1-score, Cohen's-Kappa score, ROC curve and AUC scores are calculated.

**Table 3.** TP, TN, FP, FN calculations.

	label value	prediction value
TP	positive	positive
TN	negative	negative
FP	positive	negative
FN	negative	positive

**Table 4.** Confusion matrix.

	Predicted Class: Negative	Predicted Class: Positive
Actual Class: Negative	TN	FP
Actual Class: Positive	FN	TP

**Table 5.** Calculation of Cohen's-Kappa Score parameters.

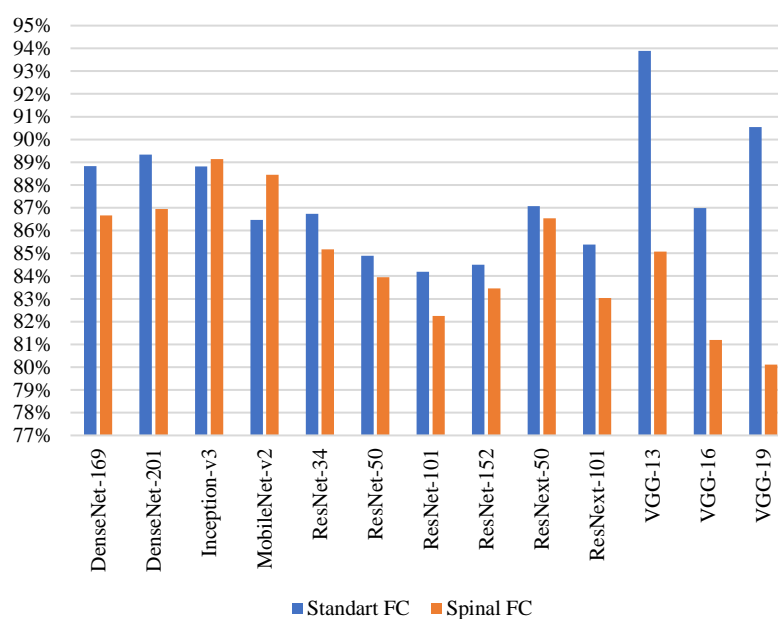
$P_0$	$(TP+TN)/(TP+TN+FP+FN)$
$P_{\text{positive}}$	$(TP+FP)(TP+FN)/(TP+TN+FP+FN)^2$
$P_{\text{negative}}$	$(FN+TN)(FP+TN)/(TP+TN+FP+FN)^2$
$P_e$	$P_{\text{positive}} + P_{\text{negative}}$

**Table 6.** Evaluation metrics.

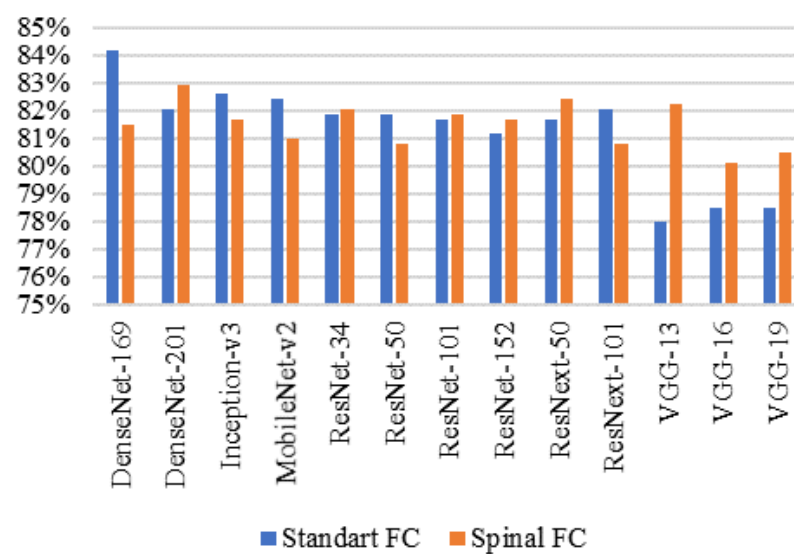
<b>Confusion Matrix</b>	TP, TN, FP, FN
<b>Training/Testing Accuracy</b>	$(TP+TN)/(TP+TN+FP+FN)$
<b>Precision</b>	$TP/(TP+FP)$
<b>Recall</b>	$TP/(TP+FN)$
<b>F1-score</b>	$2TP/(2TP+FP+FN)$
<b>Cohen-cappa score</b>	$(p_0-p_e)/(1-p_e)$
<b>ROC curve</b>	TP rate - FP rate change
<b>AUC scores</b>	Area under the ROC curve

#### 4.4.2. Classification Results of 13 CNN Based Deep Learning Models With Standart FC / Spinal FC

A total of 13 CNN models based on deep learning, including standard FC and spinal FC in their final layers, were used in classification of the shoulder bone X-ray images. The training accuracy, test accuracy, precision, recall, f1-score and Cohen's Kappa scores obtained as the result of the classification performed with each model are presented in the following figures and tables.

**Figure 21.** Training accuracy results of classification models.**Table 7.** Training accuracy results of classification models.

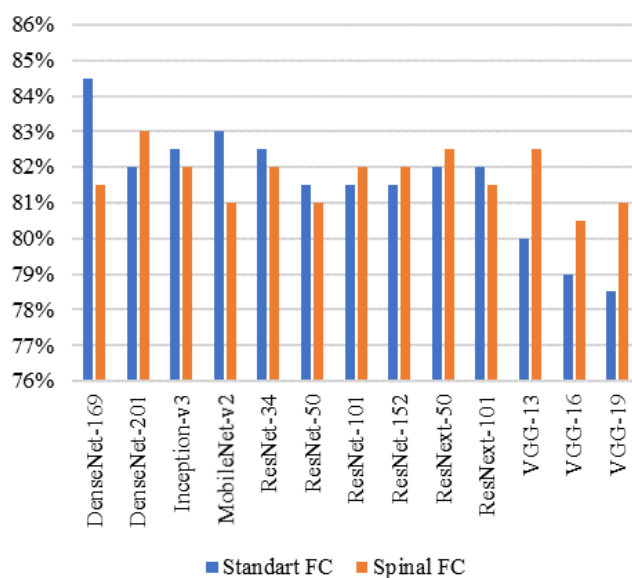
Models	Standart FC	Spinal Net	Models	Standart FC	Spinal Net
DenseNet169	0.8883	0.8666	ResNet101	0.8419	0.8225
DenseNet201	0.8934	0.8694	ResNet152	0.845	0.8346
InceptionV3	0.8882	0.8914	ResNeXt50	0.8707	0.8654
MobileNetV2	0.8647	0.8845	ResNeXt101	0.8539	0.8303
ResNet34	0.8673	0.8517	VGG13	<b>0.9389</b>	0.8507
ResNet50	0.8489	0.8395	VGG16	0.8698	0.812
			VGG19	0.9055	0.8011



**Figure 22.** Test accuracy results of classification models.

**Table 8.** Test accuracy results of classification models.

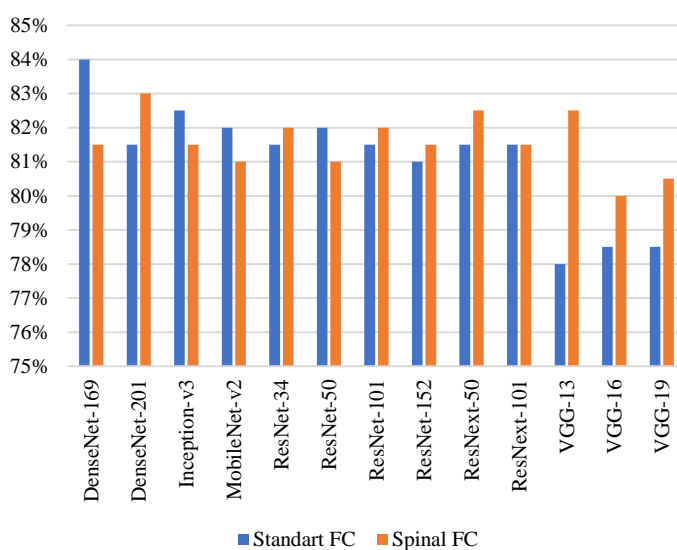
Models	Standart FC	Spinal Net	Models	Standart FC	Spinal Net
DenseNet169	<b>0.8419</b>	0.8152	ResNet101	0.817	0.8188
DenseNet201	0.8206	0.8294	ResNet152	0.8117	0.817
InceptionV3	0.8259	0.817	ResNeXt50	0.817	0.8241
MobileNetV2	0.8241	0.8099	ResNeXt101	0.8206	0.8082
ResNet34	0.8188	0.8206	VGG13	0.7797	0.8223
ResNet50	0.8188	0.8081	VGG16	0.785	0.801
			VGG19	0.785	0.8046



**Figure 23.** Precision results of classification models.

**Table 9.** Precision results of classification models.

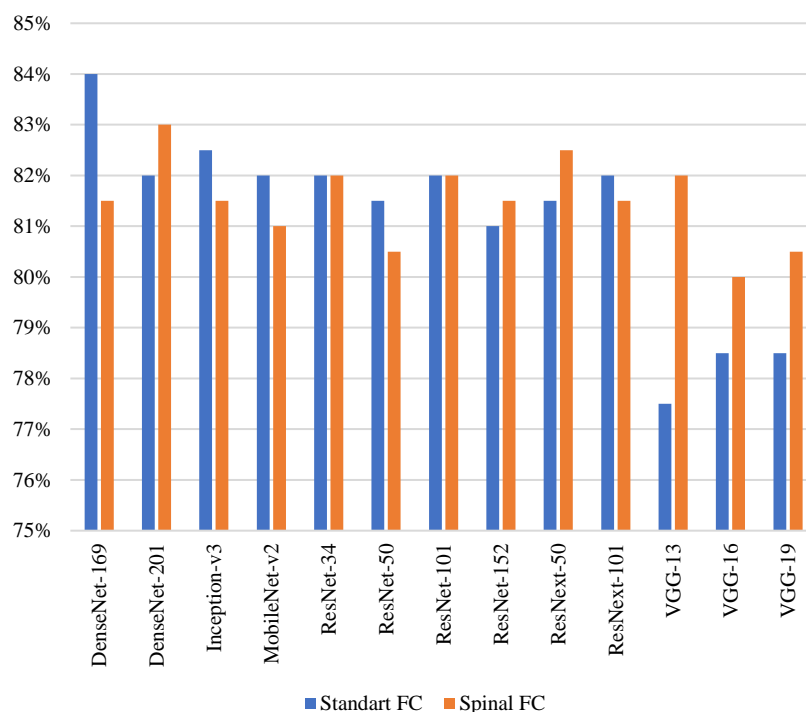
Models	Standart FC	Spinal Net	Models	Standart FC	Spinal Net
DenseNet169	<b>0.845</b>	0.815	ResNet101	0.815	0.82
DenseNet201	0.82	0.83	ResNet152	0.815	0.82
InceptionV3	0.825	0.82	ResNeXt50	0.82	0.825
MobileNetV2	0.83	0.81	ResNeXt101	0.82	0.815
ResNet34	0.825	0.82	VGG13	0.8	0.825
ResNet50	0.815	0.81	VGG16	0.79	0.805
			VGG19	0.785	0.81



**Figure 24.** Recall results of classification models.

**Table 10.** Recall results of classification models.

Models	Standart FC	Spinal Net	Models	Standart FC	Spinal Net
DenseNet169	<b>0.84</b>	0.815	ResNet101	0.815	0.82
DenseNet201	0.815	0.83	ResNet152	0.81	0.815
InceptionV3	0.825	0.815	ResNeXt50	0.815	0.825
MobileNetV2	0.82	0.81	ResNeXt101	0.815	0.815
ResNet34	0.815	0.82	VGG13	0.78	0.825
ResNet50	0.82	0.81	VGG16	0.785	0.8
			VGG19	0.785	0.805

**Figure 25.** F1-score results of classification models.**Table 11.** F1-score results of classification models.

Models	Standart FC	Spinal Net	Models	Standart FC	Spinal Net
DenseNet169	<b>0.84</b>	0.815	ResNet101	0.82	0.82
DenseNet201	0.82	0.83	ResNet152	0.81	0.815
InceptionV3	0.825	0.815	ResNeXt50	0.815	0.825
MobileNetV2	0.82	0.81	ResNeXt101	0.82	0.815
ResNet34	0.82	0.82	VGG13	0.775	0.82
ResNet50	0.815	0.805	VGG16	0.785	0.8
			VGG19	0.785	0.805



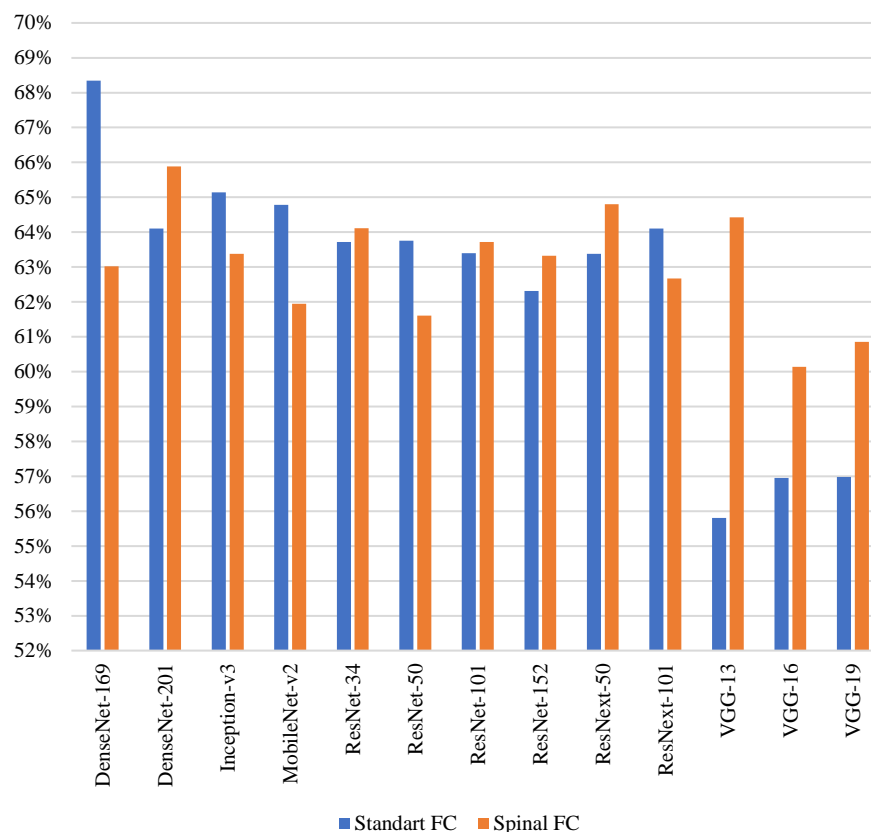


**Figure 26.** Cohen kappa results of classification models.

**Table 12.** Cohen kappa results of classification models.

Models	Standart FC	Spinal Net	Models	Standart FC	Spinal Net
DenseNet169	<b>0.6834</b>	0.6302	ResNet101	0.634	0.6372
DenseNet201	0.641	0.6588	ResNet152	0.6231	0.6332
InceptionV3	0.6514	0.6338	ResNeXt50	0.6338	0.648
MobileNetV2	0.6478	0.6195	ResNeXt101	0.641	0.6267
ResNet34	0.6372	0.6411	VGG13	0.558	0.6442
ResNet50	0.6375	0.6161	VGG16	0.5695	0.6014
			VGG19	0.5698	0.6085

It is observed upon examination of Figure 21 that the highest training accuracy achieved in classification is VGG 13 with standard FC among all the models used, and it is InceptionV3 among the models with Spinal FC. The test accuracy in figure 22, precision in figure 23, recall in figure 24, f1-score in figure 25 and Cohen's Kappa score in figure 26 conclude that the highest scores achieved are in DenseNet169 with standard FC among all the models used, and in DenseNet201 among the models with Spinal FC.

The confusion matrix values and AUC scores achieved as the result of 26 classification procedures performed with DenseNet, Inception, MobileNet, ResNet, ResNeXt and VGG models with Standard FC and Spinal FC with different number of layers are provided in table 13.

**Table 13.** Confusion matrix value and AUC score results of 26 classification models. (a: with Standart FC, b: with Spinal FC).

Models	TP	FP	FN	TN	Class0: AUC	Class1: AUC
DenseNet169a	222	33	56	252	<b>0.8809</b>	<b>0.8797</b>
DenseNet169b	218	44	60	241	0.8602	0.8598
DenseNet201a	225	48	53	237	0.8584	0.8653
DenseNet201b	228	46	50	239	0.8727	0.8724
InceptionV3a	218	38	60	247	0.8754	0.8707
InceptionV3b	220	45	58	240	0.8582	0.8585
MobileNetV2a	215	36	63	249	0.8777	0.8378
MobileNetV2b	216	45	62	240	0.8633	0.861
ResNet34a	215	39	63	246	0.8705	0.8767
ResNet34b	228	51	50	234	0.8617	0.8619
ResNet50a	224	48	54	237	0.8715	0.8662
ResNet50b	219	49	59	236	0.8588	0.8584
ResNet101a	228	53	50	232	0.8683	0.8703
ResNet101b	216	40	62	245	0.8609	0.861
ResNet152a	217	45	61	240	0.8648	0.8701
ResNet152b	220	45	58	240	0.8597	0.8606
ResNeXt50a	221	46	57	239	0.8644	0.8699
ResNeXt50b	223	44	55	241	0.8789	0.8783
ResNeXt101a	225	48	53	237	0.8772	0.8765
ResNeXt101b	219	46	59	239	0.8652	0.8561
VGG13a	181	27	97	<b>258</b>	0.8406	0.8415
VGG13b	<b>231</b>	35	65	250	0.8705	0.8737
VGG16a	203	46	75	239	0.8517	0.8523
VGG16b	204	38	74	247	0.8542	0.857
VGG19a	212	55	66	230	0.8374	0.8502
VGG19b	205	37	73	248	0.858	0.8539

It is observed upon examination of the table above that the highest classification accuracy (TP value) out of the 278 Class1 (positive, abnormal, fracture) images in the test data belongs to the VGG13 model with Spinal FC with 231 images. Moreover, out of 285 images in Class0 (negative, normal) in the test data, the highest classification accuracy (TN value) was achieved in VGG13 model with Standard FC with 258 images. It is concluded from the AUC scores in the table that the highest value in Class1 is 0.8797 and the highest value in Class0 is 0.8809. The highest AUC score achieved in both classes belongs to the DenseNet169 model with Standard FC.

In addition to the 26 classification models that were used for classification of shoulder bone X-ray images, which were explained in this section with their results, two different ensemble models were developed in the next section, which further increased the classification results.

#### 4.4.3. Classification Results of Our Ensemble Models

Based on the results of the aforementioned 13 CNN-based models used to classify the shoulder bone X-ray images as normal / abnormal (fracture), 2 different ensemble models were developed, and higher classification results were achieved. ResNeXt50 with spinal FC, DenseNet169 with standard FC and DenseNet201 with spinal FC were used in

EL1. The reasons for selection of these models among 13 CNN models for this ensemble model are as follows:

- The reason for selection of ResNeXt50 with Spinal FC is the fact that the AUC score achieved by detection of the class with the fracture images is the second highest model with 0.8783 after DenseNet169 with standard FC.
- The reason for selection of DenseNet169 with standard FC is the fact that the classification has the highest test accuracy, Cohen's Kappa score and AUC score among all models used in this study.
- The reason for selection of DenseNet201 with Spinal FC is the fact that examination of the test accuracy and Cohen's Kappa scores reveal that it is the second highest model after DenseNet169 with Standard FC and the highest model among models with Spinal FC.

The results achieved by the classification performed using the EL1 model are provided in the following figures and tables. In table 14, ResNeXt50b represents ResNeXt50 model with Spinal FC, and DenseNet169a represents DenseNet169 model with standard FC, and DenseNet201b represents DenseNet201 model with Spinal FC.

**Table 14.** Classification results of EL1.

Models	Test acc.	Pre.	Recall	F1-score	Cohen kappa
ResNeXt50b	0.8241	0.825	0.825	0.825	0.648
DenseNet169a	0.8419	0.845	<b>0.84</b>	0.84	0.6834
DenseNet201b	0.8294	0.83	0.83	0.83	0.6588
EL1	<b>0.8455</b>	<b>0.8631</b>	0.8165	<b>0.8455</b>	<b>0.6907</b>

It is observed upon examination of the table above is that the test accuracy is 0.8455 and Cohen's Kappa score is 0.6907 with the EL1 model. Therefore, the highest classification result obtained with DenseNet169 with Standard FC in the previous section was exceeded.

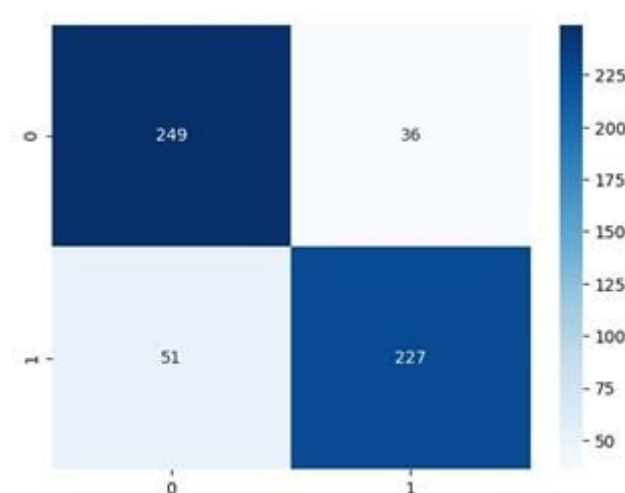


**Figure 27.** Confusion matrix results of EL1.

The confusion matrix specified in the figure above was achieved as the result of the classification performed using the EL1 model. The following results are concluded as per the figure; TN: 249, FP: 36, FN: 51 and TP: 227.

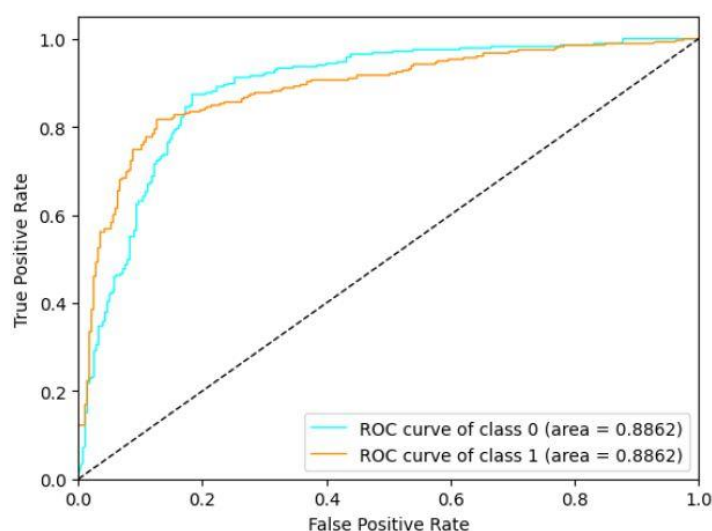


**Figure 28.** ROC curves and AUC results of EL1.

ROC curves and AUC scores achieved by the classification performed with the EL1 model are presented in the figure above. It is concluded from the ROC curve representing the change of TP rate and FP rate of this model that an AUC score of 0.8862 is achieved for class 0 (normal) and class 1 (abnormal, fracture). This AUC score is also higher than the AUC achieved with ResNet169 with Spinal FC in the previous section.

3 different single classification models and an sub-ensemble model were used in the EL2 model. These are; ResNet34 with Spinal FC, DenseNet201, DenseNet169 with Standard FC and sub-ensemble models. The TP and TN values in the Confusion Matrix scores and recall scores from the 26 different classification models used in the first stage were taken into consideration while choosing the 3 single models used in the EL2 model and developing the sub-ensemble model. The results of the classification carried out with the EL2 model are provided in the table below. In table 15; ResNet34b represents ResNet34 model with Spinal FC, DenseNet169a represents DenseNet169 model with Standard FC, DenseNet201b represents DenseNet201 model with Spinal FC, and SubEnsemble represents sub-ensemble model developed.

**Table 15.** Classification results of EL2.

Models	Test acc.	Pre.	Recall	F1-score	Cohen kappa
ResNet34b	0.8206	0.82	0.82	0.82	0.6411
DenseNet169a	0.8419	0.815	0.84	0.84	0.6834
DenseNet201b	0.8294	0.83	0.83	0.83	0.6588
SubEnsemble	0.8401	0.84	0.84	0.84	0.6799
EL2	<b>0.8472</b>	<b>0.85</b>	<b>0.845</b>	<b>0.845</b>	<b>0.6942</b>

It is observed upon examination of the table above providing the results of classification with the EL2 that Cohen's Kappa is achieved as 0.6942 and the test accuracy score is achieved as 0.8472. These results show that the highest result was achieved in the EL2 model when compared to the classification results achieved with the 26 CNN-based models and EL1 model within the scope of this study.

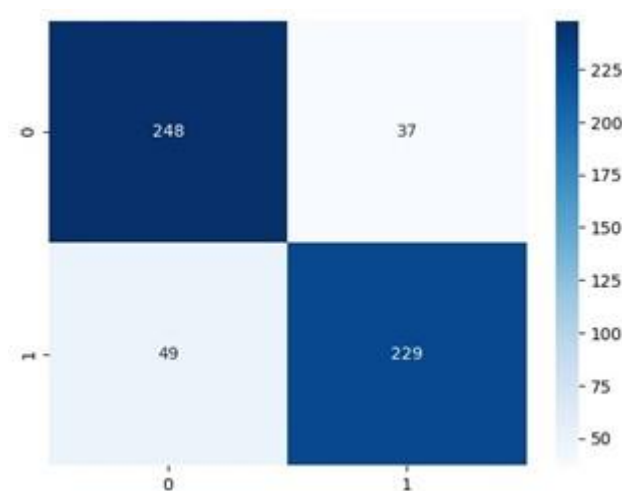


**Figure 29.** Confusion matrix results of EL2.

The figure above presents the confusion matrix scores achieved as the result of the classification carried out with the EL2 model. It is observed upon examination of the figure that the following results have been obtained; TN: 248, FP: 36, FN: 49 and TP: 229. The comparison of these results with the EL1, in particular, shows that the number of detection (TP) of images with shoulder bone fracture in the EL1 model was 227, while this result increased to 229 in the EL2 model.

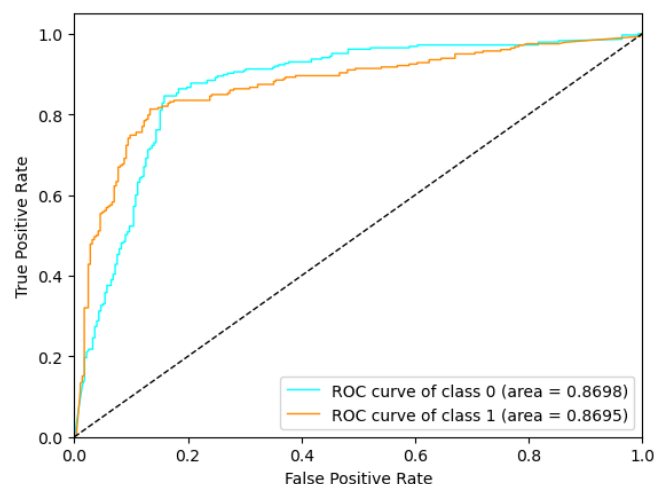


**Figure 30.** ROC curves and AUC results of EL2.

The ROC curves and AUC scores achieved as the result of the classification performed with the EL2 model are provided in the figure above. It is observed upon examination of the figure that AUC scores achieved are 0.8698 for Class0 (normal, negative) and 0.8695 for Class1 (abnormal, positive, fracture). Although these AUC scores appear to be slightly decreased compared to the EL1 model, due to the fact that the test accuracy, Cohen's Kappa scores, and the number of images with shoulder bone fracture (in TP) achieved in the EL2 model are higher than the EL1 model, it is possible to state that the classification procedure carried out by the EL2 model within the scope of this study provides better results.

## 5. Conclusion and Future Work

The aim of this study was to find the most optimum model by classifying shoulder bone X-ray images as normal / abnormal (fracture). In order to achieve such aim, the first objective was to find fracture images on 26 classification models, comprised of 13 different CNN-based models, with each having standard FC and spinal FC versions. Based on the results obtained therein, 2 different ensemble models (EL1 and EL2) were developed and used for classification procedures carried out in order to further increase the classification accuracy and Cohen's Kappa score. As the result of a total of 28 different classifications carried out, the highest test accuracy and Cohen's Kappa score were achieved in the EL2 model, and the highest AUC score was achieved in the EL1 model. The contribution of the study to the literature is as follows.

- It has been observed that mostly the binary classification is performed in similar studies conducted in the literature. On the other hand, while there are mainly two classes (normal / abnormal) in this study, differently from the literature, multi-class classification has been carried out instead of binary classification. The reason thereof is to determine the most compatible models to be used in ensemble models developed by evaluating the outputs of each class of 26 classification models conducted initially. This allowed the best results in this classification study to be achieved with ensemble models.
- Another innovation introduced to the literature is that this is the first time that Spinal FC, which has a lower number of weights in the hidden layer compared to the standard FC in the classification layers of the models, was used in many models (Inception, ResNeXt, MobileNet) within the scope of this study. Moreover, SpinalNet was used on medical images for the first time; and it is observed upon examination of these models using SpinalNet that it had a positive effect on the classification results in more than half of them.
- A unique structure that will contribute to the literature has been introduced since the reliability of detection of class was used as basis while designing the EL2 model, one of the ensemble models developed to further increase the classification results.

The aim of this study, which enables detection of images of fracture through classification of the shoulder bone X-ray images, is to help physicians diagnose fractures in the shoulder and apply the required treatment. Following the study, a real-time mobile application that detects the fracture image and / or the fracture area for the shoulder bones can be developed in order to help physicians in emergency services in particular.

**Author Contributions:** Conceptualization, F.U., F.H. and O.P.; methodology, F.U., F.H. and O.P.; software, F.U., F.H. and O.P.; validation, F.U., F.H. and O.P.; formal analysis, F.U., F.H. and O.P.; investigation, F.U., F.H. and O.P.; resources, F.U., F.H. and O.P.; data curation, F.U., F.H. and O.P.; writing—original draft preparation, F.U., F.H. and O.P.; writing—review and editing, F.U., F.H., O.P., T.T. and N.T.; visualization, F.U., F.H. and O.P.; supervision, F.U., F.H. and O.P. All authors have read and agreed to the published version of the manuscript.

**Funding:** This research received no external funding.

**Institutional Review Board Statement:** Not applicable.

**Informed Consent Statement:** Not applicable.

**Data Availability Statement:** Data used in this study is available at <https://stanford-mlgroup.github.io/competitions/mura>.

**Conflicts of Interest:** The authors declare no conflict of interest.

## References

1. Shoulder Fracture 2014. Available online: <https://www.assh.org/handcare/condition/shoulder-fracture> (accessed on 1 September 2020).
2. Rajpurkar, P.; Irvin, J.; Bagul, A.; Ding, D.; Duan, T.; Mehta, H.; Yang, B.; Zhu, K.; Laird, D.; Ball, R.L.; Langlotz, C.; Shpanskaya, K.; Lungren, M.P.; Ng, A.Y. MURA Dataset: Towards Radiologist-Level Abnormality Detection in Musculoskeletal Radiographs. 1st Conference on Medical Imaging with Deep Learning, Amsterdam, The Netherlands, June 2018.
3. Guan, B.; Zhang, G.; Yao, J.; Wang, X.; Wang, M. Arm fracture detection in X-rays based on improved deep convolutional neural network. *Computers and Electrical Engineering* **2020**, *81*, 1–11.
4. Galal, A.; Hisham, F.; Mohamed, M.; Hassan, S.; Ghanim, T.; Nabil, A. Automatic Recognition of Elbow Musculoskeletal Disorders using Cloud Application. Proceedings of the 2019 8th International Conference on Software and Information Engineering, Cairo, Egypt, 2019.
5. Liang, S.; Gu, Y. Towards Robust and Accurate Detection of Abnormalities in Musculoskeletal Radiographs with a Multi-Network Model. *Sensors* **2020**, *20*, 3153.
6. Saif, A.F.M.; Shahnaz, C.; Zhu, W.P.; Ahmad, M.O. Abnormality Detection in Musculoskeletal Radiographs Using Capsule Network. *IEEE Access* **2019**, *7*, 81494–81503.
7. Cheng, K.; Iriondo, C.; Calivá, F.; Krogue, J.; Majumdar, S.; Pedoia, V. Adversarial Policy Gradient for Deep Learning Image Augmentation. Proceedings of 22nd International Conference on Medical Image Computing and Computer Assisted Intervention, Shenzhen, China, 2019.
8. Pelka, O.; Nensa, F.; Friedrich, C.M. Branding - Fusion of Meta Data and Musculoskeletal Radiographs for Multi-modal Diagnostic Recognition. Proceedings of the IEEE/CVF International Conference on Computer Vision Workshop, Seoul, Korea, 2019.
9. Varma, M.; Lu, M.; Gardner, R.; Dunnmon, J.; Khandwala, N.; Rajpurkar, P.; Long, J.; Beaulieu, C.; Shpanskaya, K.; Fei-Fei, L.; Lungren, M.P.; Patel, B.N. Automated abnormality detection in lower extremity radiographs using deep learning. *Nature Machine Intelligence* **2019**, *1*, 578–583.
10. Harini, N.; Ramji, B.; Sriram, S.; Sowmya, V.; Soman, K.P. Musculoskeletal radiographs classification using deep learning. In *Deep Learning for Data Analytics: Foundations, Biomedical Applications and Challenges*, 1st ed.; Das, H.; Pradhan, C.; Dey N., Eds.; Academic Press: United Kingdom, 2020; pp. 79–98.
11. Fang, L.; Jin, Y.; Huang, L.; Guo, S.; Zhao, G.; Chen, X. Iterative fusion convolutional neural networks for classification of optical coherence tomography images. *J. Vis. Commun. Image R.* **2019**, *59*, 327–333.
12. Mondol, T.C.; Iqbal, H.; Hashem, M. Deep CNN-Based Ensemble CADx Model for Musculoskeletal Abnormality Detection from Radiographs. Proceedings of the 2019 5th International Conference on Advances in Electrical Engineering, Dhaka, Bangladesh, 2019.
13. Pradhan, N.; Dhaka, V.S.; Chaudhary, H. Classification of Human Bones Using Deep Convolutional Neural Network. IOP Conference Series: Materials Science and Engineering, International Conference on Startup Ventures: Technology Developments and Future Strategies, Rajasthan, India, 2019.
14. Shao, Y.; Wang, X. A Two Stage Method for Abnormality Diagnosis of Musculoskeletal Radiographs. Proceeding of the International Conference on Pattern Recognition and Artificial Intelligence, Zhongshan, China, 2020.
15. Chung, S.W.; Han, S.S.; Lee, J.W.; Oh, K.S.; Kim, N.R.; Yoon, J.P.; Kim, J.Y.; Moon, S.H.; Kwon, J.; Lee, H.J.; Noh, Y.M.; Kim, Y. Automated detection and classification of the proximal humerus fracture by using deep learning algorithm. *Acta Orthopaedica* **2018**, *89*, 468–473.
16. Sezer, A.; Sezer, H.B. Convolutional neural network based diagnosis of bone pathologies of proximal humerus. *Neurocomputing* **2020**, *392*, 124–131.
17. Urban, G.; Porhemmat, S.; Stark, M.; Feeley, B.; Okada, K.; Baldi, P. Classifying shoulder implants in X-ray images using deep learning. *Computational and Structural Biotechnology Journal* **2020**, *18*, 967–972.
18. Sezer, A.; Sigirci, I.O.; Sezer, H.B. Shoulder lesion classification using shape and texture features via composite kernel. 25th Signal Processing and Communications Applications Conference (SIU), Antalya, 2017.
19. Sezer, A.; Sezer, H.B. Capsule network-based classification of rotator cuff pathologies from MRI. *Computers and Electrical Engineering* **2019**, *80*, 106480.
20. Russakovsky, O.; Deng, J.; Su, H.; Krause, J.; Satheesh, S.; Ma, S.; Huang, Z.; Karpathy, A.; Khosla, A.; Bernstein, M.; Berg, A.C.; Fei-Fei, L. ImageNet Large Scale Visual Recognition Challenge. *International Journal of Computer Vision* **2015**, *115*, 211–252.
21. He, K.; Zhang, X.; Ren, S.; Sun, J. Deep Residual Learning for Image Recognition. IEEE Conference on Computer Vision and Pattern Recognition (CVPR), Las Vegas, NV, 2016.
22. Xie, S.; Girshick, R.; Dollár, P.; Tu, Z.; He, K. Aggregated Residual Transformations for Deep Neural Networks. IEEE Conference on Computer Vision and Pattern Recognition (CVPR), Honolulu, HI, 2017.
23. Huang, G.; Liu, Z.; Van Der Maaten, L.; Weinberger, K.Q. Densely Connected Convolutional Networks. IEEE Conference on Computer Vision and Pattern Recognition (CVPR), Honolulu, HI, 2017.
24. Simonyan, K.; Zisserman, A. Very deep convolutional networks for large-scale image recognition. *arXiv* **2014**, arXiv:1409.1556.

25. Szegedy, C.; Vanhoucke, V.; Ioffe, S.; Shlens, J.; Wojna, Z. Rethinking the Inception Architecture for Computer Vision. *IEEE Conference on Computer Vision and Pattern Recognition (CVPR)*, Las Vegas, NV, 2016.
26. Sandler, M.; Howard, A.; Zhu, M.; Zhmoginov, A.; Chen, L. MobileNetV2: Inverted Residuals and Linear Bottlenecks. *IEEE/CVF Conference on Computer Vision and Pattern Recognition*, Salt Lake City, UT, 2018.
27. Kabir, H.M.D.; Abdar, M.; Jalali, S.M.J.; Khosravi, A.; Atiya, A.F.; Nahavandi, S.; Srinivasan, D. SpinalNet: Deep neural network with gradual input. *arXiv* **2020**, arXiv:2007.03347.
28. Otsu, N. A Threshold Selection Method from Gray-Level Histograms. *IEEE Transactions on Systems, Man, and Cybernetics* **1979**, 9, 62-66.
29. Pizer, S.M.; Johnston, R.E.; Ericksen, J.P.; Yankaskas, B.C.; Muller, K.E. Contrast-limited adaptive histogram equalization: speed and effectiveness. *Proceedings of the First Conference on Visualization in Biomedical Computing*, Atlanta, GA, USA, 1990.
30. Zuiderveld, K. Contrast limited adaptive histogram equalization. In *Graphics Gems IV*, Heckbert, P.S., Eds.; Academic Press Professional: San Diego, CA, United States, 1994, pp. 474-485, 1994.